IEEE Access
Multidisciplinary ⋮ Rapid Review ⋮ Open Access Journal

Received February 4, 2021, accepted February 17, 2021, date of publication February 26, 2021, date of current version March 9, 2021.

Digital Object Identifier 10.1109/ACCESS.2021.3062663

Vision-Based Position Deviation Measurement of Rail Corrugation Chord Measuring Points Under Bi-Linear Laser Assistance

LIANG CHEN[1], YANFU LI[2], ZIJI MA[3], HONGLI LIU[3], AND WEIJIE MAO[1]

[1]State Key Laboratory of Industrial Control Technology, Institute of Cyber-Systems and Control, Zhejiang University, Hangzhou 310027, China
[2]Information and Navigation College, Air Force Engineering University, Xi'an 710077, China
[3]College of Electrical and Information Engineering, Hunan University, Changsha 410082, China

Corresponding author: Weijie Mao (wjmao@zju.edu.cn)

This work was supported in part by the National Natural Science Foundation of China under Grant 61633019, Grant 61771191, and Grant 61971182; and in part by the Changsha City Science and Technology Department Funds under Grant KQ1801194.

ABSTRACT During the dynamic measurement of chord-based rail corrugation, with the interferences of curve rail and train snaking movement, it is hard to ensure that the measuring points on the rail surface can trace the railhead centerline well the whole time. This introduces the position deviations to the measurement system, and leads to the measurement results cannot reflect the true rail irregularity state. To solve the problem, a position deviation measurement method based on the assistance of bi-linear laser is proposed in this paper. First, by means of three verifications composed of color, dimension and position, the laser stripe regions on railhead are located from original image effectively. Then, by suppressing stripe highlight texture and modifying the traditional Steger algorithm with flexible-widths Gaussian template, we extract the laser stripe centerline accurately, and depict the railhead boundary fast. Last, by locating three chord-based measuring points and calculating the distances from them to the railhead centerline, we obtain the position deviations of each point. The efficiency and superiority of proposed method are verified by vast experiments. The results show that the accuracy of the position deviation of the chord-based measuring points is limited within 0.4mm.

INDEX TERMS Bi-linear laser assistance, chord-based method, vision-based measurement, position deviation, rail corrugation.

I. INTRODUCTION

Rail corrugation which is caused by wheel–rail interactions and occurs on rail top surfaces along the track longitudinal axis is a vertical track irregularity phenomenon [1], [2]. It has been one of the main damages for urban mass transit. Severe corrugation not only shortens rail service life, but also excites harsh noise, and can even lead to disasters [3], [4]. Hence, the accurate and effective measurement and schedule maintenance are very necessary for alleviating rail corrugation [5].

A. RAIL CORRUGATION MEASUREMENT METHODS

The rail corrugation measurement method can be divided into two types: contact measurement and non-contact measurement. The contact measurement usually uses a ruler to manually measure the surface irregularity of the rail. Contact measurement is still widely used due to its convenience, in spite of its limited measurement range or relatively low accuracy. The non-contact measurement method that have two popular types: inertial reference method and chord-based method, needs to be mounted on a kind of car or train for automatic measurement [6], [7].

Inertial reference method acquires the vibration acceleration signal to monitor the rail corrugation [8]. The simple lumped parameter model of the wheel rail system is shown in Figure 1(a). According to the dynamic principle, we can get the relationship between rail corrugation and acceleration recorded by an accelerometer installed on the bogie or axle box of the train. From that, we can see that the frequency of acceleration is the same as the frequency of rail corrugation. It is the quadratic differential of rail corrugation. So we can get the rail corrugation by double integration if we have

The associate editor coordinating the review of this manuscript and approving it for publication was Xinyue Xu.

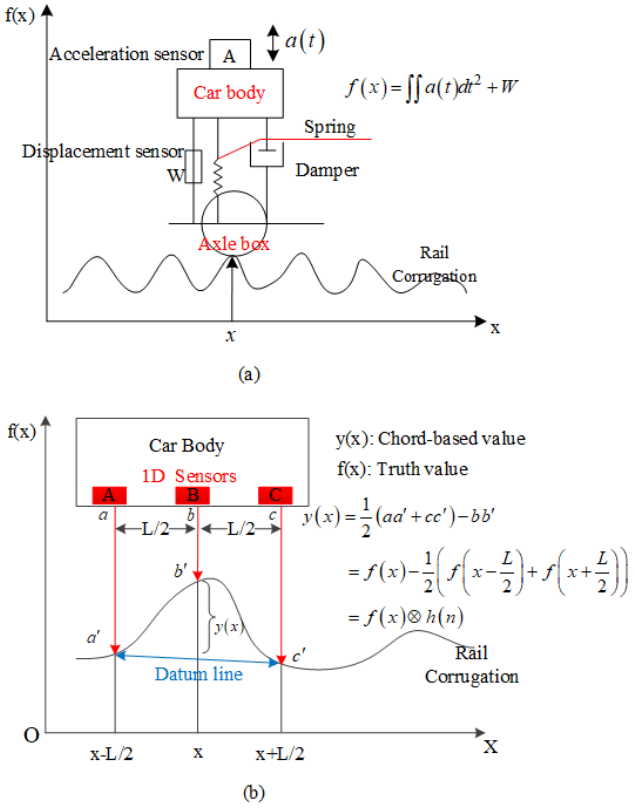

FIGURE 1. Schematic diagram of three-point symmetrical chord method.

detected the vertical axle-box acceleration of the train using an accelerometer. However, the variable vehicle speed may cause the drift of platform reference. It introduces measurement error to the inertial measuring system [9].

Taking the three-point symmetrical chord method (3SCM) as an example, the schematic diagram is shown in Figure 1(b). Three 1D laser displacement sensors numbered from A to C are fixed at the bottom of the carriage. They are arranged along the track longitudinal axis, and the interval is equal to half of the chord length L. Provided that three laser reflection points on the rail surface are a', b' and c', respectively. The chord is supported by the first and the third detecting points on the rail, and the distance from the middle detecting point b' to the chord $a'c'$ is taken as the chord-based measurement value $y(x)$. Then, with a corresponding inverse filtering, the real rail corrugation is acquired [10]. The effective waveband of measurable corrugation for 3SCM is $L/2 < \lambda \leq 7L$. Compared with the other methods, such as the inertia reference method, the most significant advantage of chord-based method is that the result is robust to the vehicle speed [11]. Our research is based on the chord-based method.

B. CHALLENGES FOR CHORD-BASED METHOD

According to the measurement rule [12], [13], the positions of three measuring points should be located near the railhead centerline within a scope of ±10 mm. However, during the process of dynamic measurement, it is hard to meet this

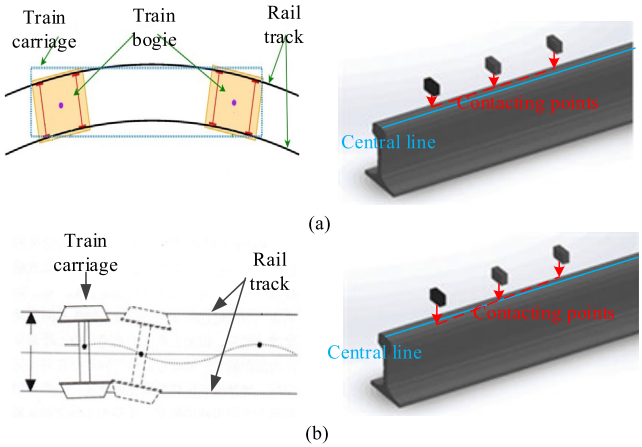

FIGURE 2. Challenge of chord-based method. (a) Curve rail. (b) Snaking motion.

condition the whole time, because of the following factors. First is the influence of curve rail. As shown in Figure 2(a), when cross the curve rail, the train bogies move along in the curve track. The train carriage will find horizontal deviations. At this time, the line of measuring points will move to the railhead edge synchronously. Second is the influence of snaking motion. As shown in Figure 2(b), with the improvement of train speed and the existence of rail irregularity, the carriage axial direction changes frequently during the process of moving forward. This causes that the line of measuring points could incline to the railhead centerline.

C. RELATED WORK

The existence of position deviations of measuring points makes the measurement results cannot reflect the true rail irregularity state. To solve this problem, Li *et al.* [14] present a chord-based points correction system by the real-time change of the track gauge. This system simultaneously adjusts the position of the sensors on both ends to correct the gauge changes. However, the measurement method is poor accuracy, because it is not clear how much the position deviations between each sensor and effective measurement region. An effective method has been proposed in the literature [15]. By extracting the railhead boundary from the sophisticated edge image and locating the laser measuring points, they calculate the position deviation of each point accurately. However, this method is sensitive to the illumination and reflection property on the rail surface. To weaken the sensitivity, we have to add additional light source and take measures to enhance the image contrast. Thus makes the complexity of this method becomes higher.

D. OUTLINE OF OUR WORK

To address the issue mentioned above, we adopt the bi-linear laser to locate the railhead boundary and measure the position deviation in this paper. The contributions are summarized in the following.

1) To improve the performance of previous method, we adopt the bi-linear laser to locate the railhead boundary

TABLE 1. Designation and specification of used components.

No	Designation	Specification
1	Stepping motor	Move the sensor with the speed of 7.5mm/s
2	ZSY1D laser displacement sensor	Measure the vertical displacement with distinguishability 0.001mm
3	Encoder	Provide the mileage information and trig the sampling of sensors
4	Battery	Provide the Power
5	Computer	Data processing and calculation
6	MGS130-H color planar array CCD camera	Filming the testing area
7	Bi-linear laser	Assisting to extract the rail boundary

and measure the position deviation in this paper. Compared with the previous method, the most significant breakthrough is that this method is insensitive to the illumination and reflection property of the rail surface. Thus makes it could work day and night, without the assistance of additional light source.

2) In addition, we modify the traditional Steger algorithm with flexible-widths Gaussian template. Thus makes the extraction of laser stripe centerline and railhead boundary more accurate.
3) Comprehensive experiments show the effectiveness and superiority of new method. The accuracy of the position deviation measurement is limited within 0.4 mm. Compared with Graph Cuts and edge detection, our method is more stable, accurate and feasible.

The paper is organized as follows: the overview of the measuring system is described briefly in Section II. Section III describes the process of position deviation measurement under the assistance of bi-linear laser. Section IV provides the experiment. Finally, the conclusion of this paper is drawn in Section V.

II. SYSTEM CONSTRUCTION

The schematic diagram of position deviation measurement system under bi-linear laser assistance is shown in Figure 3. It is mainly composed of a position monitoring subsystem and a position correction subsystem. When the train is running, the low frequency pulse drives the area-array camera to monitoring the chord-based measuring points in real-time. Then, the deviations are corrected by the stepping motor. In this paper, we focus on position deviation monitoring subsystem. The hand-push rail corrugation measurement platform shown in Figure 4. The designation and specification of relative components are listed in Table 1. The chord length L of the hand-push rail corrugation measurement platform is 1m. the effective waveband of measurable corrugation is $0.5\text{m} < \lambda \leq 7\text{m}$.

To construct the coordinate system of the position of the chord-based measuring points, Chen *et al.* [15] present the geometric position of railhead boundary as the consult position, which is located on the intersection point between railhead arc and the inner line whose slope is 1:20. The vertical

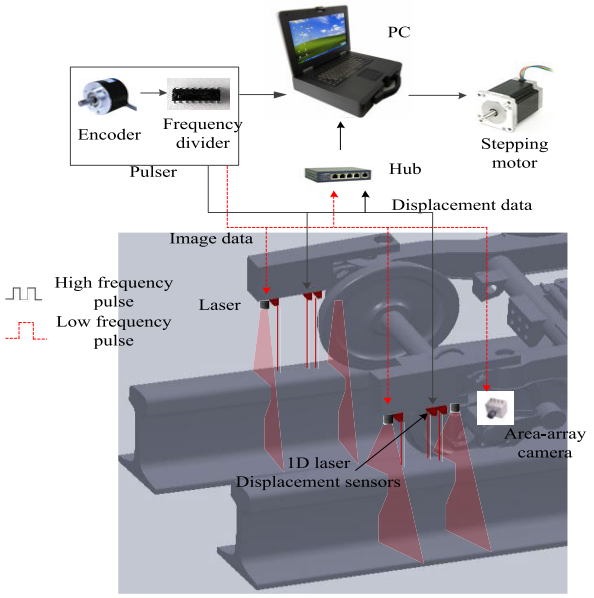

FIGURE 3. Schematic diagram of position deviation measurement system.

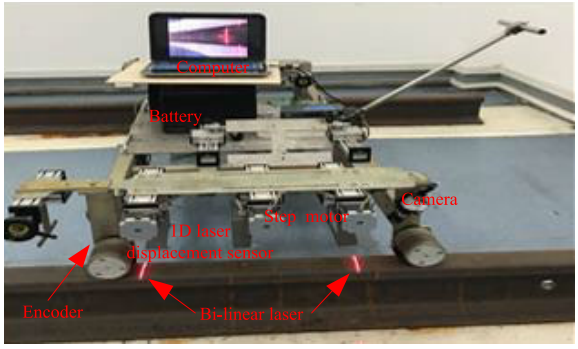

FIGURE 4. Hand-push rail corrugation measurement platform.

distance and transverse distance of railhead boundary from the railhead midline are 14.2mm and 35.4mm respectively.

III. POSITION DEVIATION MEASUREMENT UNDER BI-LINEAR LASER ASSISTANCE

The process of position deviation measurement under bi-linear laser assistance is shown in Figure 4. It includes the extraction of effective laser stripe region, suppression of stripe highlight texture, extraction of stripe centerline, railhead boundary definition, location of laser measuring points and deviation measurement. Next, we will account for them one by one.

A. EXTRACTION OF EFFECTIVE LASER STRIPE REGION

As shown in Figure 5, the outer ring of laser regions appears red, while the inner part appears bright white color with the increasement of luminosity. It is located on the rail surface, and presents a long stripe along the gauge direction. Inspired by these features, a coarse-to-fine process for the location of laser stripe region is described as follows.

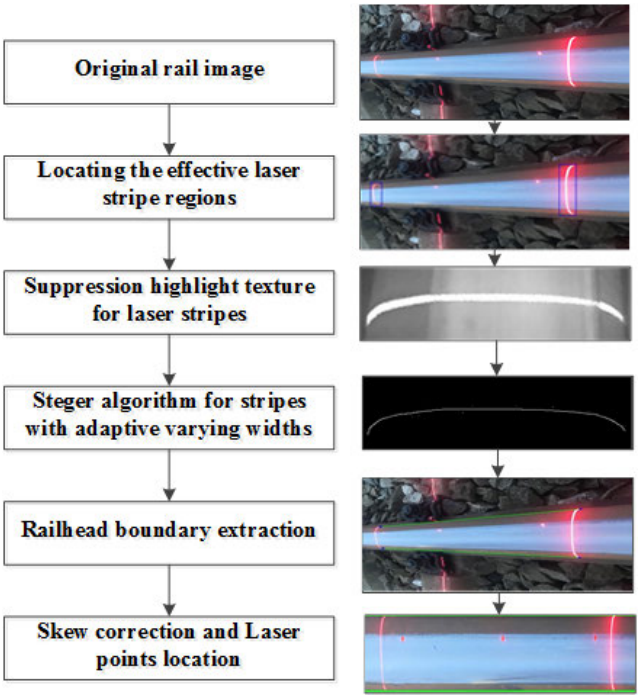

FIGURE 5. Operation process.

1) COLOR VERIFICATION OF LASER STRIPE REGIONS

Search the original color image I_c by lines along the rail direction according to the given red threshold range $T_r = \{R > 215, G < 185, B < 200\}$. For the i_{th} line, denote the positions of start pixel and stop pixel meeting the condition as i_s and i_e. If $i_e - i_s < \alpha \cdot I_{width}$, let $I_{bw} = (i_s : i_e, i_{\text{th}}) = 1$, where I_{bw} is a zero matrix with the same dimension as I_c. I_{width} represents the width of this image, and α is the ratio coefficient. Here, α is set as 0.005. After the first search, there are some rusty spots and debris left. To remove these interferences, the second verification of laser stripes centroids is performed with preset white threshold range $T_w = \{R > 250, G < 240, B < 240\}$. The result and the binary image of color verification are shown in Figure 6(a) and (b).

2) DIMENSION VERIFICATION OF LASER STRIPE REGIONS

After the search, process I_{bw} with an area opening operation to merge the short discontinuous laser stripes segments together. According to the characteristics of railhead laser stripes, the geometric dimension of the smallest rectangles on the effective laser stripe regions should meet the following empirical conditions:

$$R_{height} > \beta \cdot I_{width} \tag{1}$$

where R_{height} represents the height of the smallest rectangle, β is the ratio coefficient, Here, β is set as 0.15. The result of dimension verification is shown in Figure 6(c).

3) POSITION VERIFICATION OF LASER STRIPE REGIONS

After the color and dimension verification, there are countable laser stripe regions left on the image generally.

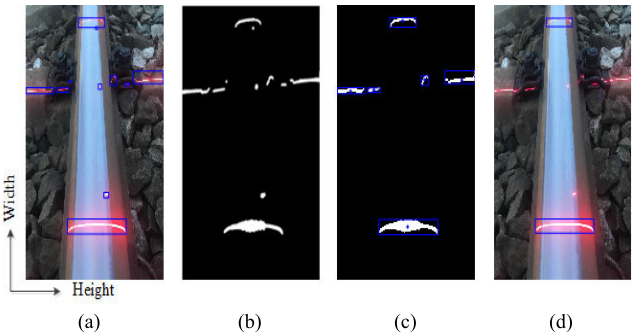

FIGURE 6. Three verifications for the location of laser stripe region. (a) Color verification. (b) Binary image of color verification. (c) Dimension verification. (d) Position verification.

The relative position between the laser stripe regions is adopted here for the final position verification.

First, we get the centroid of each laser stripe regions. Second, for measuring the relative position of each laser stripe region, the Euclidean distance D_{ij} between the laser stripe regions are obtained.

$$D_{ij} = \sqrt{\left(x_i - x_j\right)^2 + \left(y_i - y_j\right)^2} \tag{2}$$

where (x_i, y_i) and $\left(x_j, y_j\right)$ are the centroid coordinates of two laser stripe regions in the image, respectively. Obviously, the Euclidean distance of the effective laser stripe regions on the railhead surface is the maximum. The result of position verification is shown in Figure 6(d).

B. SUPPRESSION OF STRIPE HIGHLIGHT TEXTURE

The smooth wheel-rail contact areas reflect more light than the other oxidized parts. As shown in Figure 6(a), thus could increase some highlight textures in these areas, and influences the extraction of stripe centerline. Hence, we need to take measures to suppress these highlight textures.

Gabor energy operator [16] is a kind of feature that can be used to describe image texture information. It comes from the model of the Gabor filter. The two-dimensional expression of Gabor filter in the time domain is shown as follows:

$$\begin{aligned} &h\left(x, y\right) \\ &= g\left(x\cos\theta + y\sin\theta, -x\sin\theta + y\cos\theta\right) e^{j2\pi F\left(x\cos\theta + y\sin\theta\right)} \end{aligned} \tag{3}$$

where θ is the azimuth angles, F is the center frequency of filter, and $g(x, y)$ is the Gaussian function.

Gabor energy operator can be expressed as:

$$E_g\left(x, y; \theta\right) = \sqrt{E_e^2\left(x, y; \theta\right) + E_o^2\left(x, y; \theta\right)} \tag{4}$$

$$E_e^2\left(x, y; \theta\right) = I\left(x, y\right) * h_e\left(x, y; \theta\right) \tag{5}$$

$$E_o^2\left(x, y; \theta\right) = I\left(x, y\right) * h_o\left(x, y; \theta\right) \tag{6}$$

where $h_e\left(x, y; \theta\right)$ and $h_o\left(x, y; \theta\right)$ are the real and imaginary parts of the two-dimensional Gabor function, respectively.

The edge pixels in the original region are detected efficiently using Gabor energy operators with different azimuth

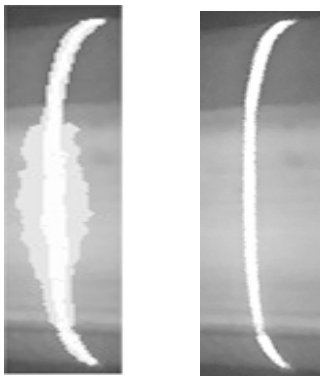

(a) (b)

FIGURE 7. Suppression of stripe highlight texture. (a)Original stripe. (b)Processed stripe.

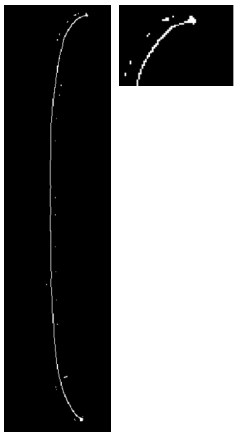

FIGURE 8. Extraction of laser stripe centerline by traditional Steger algorithm.

angles. These edges are the embodiment of a sharp change in gray scale, without any prior knowledge of profile and neighborhood influence. Therefore, the theory of surround suppression based on the model of non-classical receptive field is proposed to make the edge of the stripe profile prominent in the extracted minimum laser stripe region.

The orientation and distance of surround pixels may cause the change of the Gabor energy response. The same orientation has a strong inhibitory effect on the response, whereas the suppression effect is less. Meanwhile, the farther the distance is, the smaller the suppression effect is. This distance action can be simulated by the differential Gaussian function $DoG_\sigma(x, y)$.

$$DoG_\sigma(x, y) = \frac{1}{\sqrt{2\pi}(k\sigma)^2} e^{\frac{x^2+y^2}{2(k\sigma)^2}} - \frac{1}{\sqrt{2\pi\sigma^2}} e^{\frac{x^2+y^2}{2\sigma^2}} \quad (7)$$

where k is the standard deviation ratio, and is usually set as 2. Then, the weight function $w_\sigma(x, y)$ can be defined as:

$$w_\sigma(x, y) = \frac{H(DoG_\sigma(x, y))}{\|H(DoG_\sigma(x, y))\|} \quad (8)$$

where $H(z) = \begin{cases} 0, z < 0 \\ z, z > 0 \end{cases}$.

The suppression term $s_\sigma(x, y)$ can be expressed as:

$$s_\sigma(x, y) = E_g(x, y; \theta) \otimes w_\sigma(x, y) \quad (9)$$

When considering surround suppression, Gabor energy can be expressed as

$$E_{gs}(x, y; \theta) = H\left(E_g(x, y; \theta) - \alpha s_\sigma(x, y)\right) \quad (10)$$

Taking the stripe image shown in Fig. 7(a) as an example, the result after surround suppression is shown in Figure 7(b). Obviously, the influence of highlight texture is weakened effectively.

C. EXTRACTION OF LASER STRIPE CENTERLINE WITH MODIFIED STEGER ALGORITHM

In order to obtain the railhead boundary, we should extract the endpoints of each laser stripe. To obtain the most accurate pixel information of the endpoints, we extract the centerline of the laser stripe by Steger algorithm. The process is described as follows:

1) Figure out the normal direction of the stripe centerline through the Hessian matrix.

$$H(x, y) = \begin{pmatrix} \frac{\partial^2 g(x,y)}{\partial x^2} & \frac{\partial^2 g(x,y)}{\partial x \partial y} \\ \frac{\partial^2 g(x,y)}{\partial x \partial y} & \frac{\partial^2 g(x,y)}{\partial y^2} \end{pmatrix} \otimes Z(x, y) = \begin{pmatrix} r_{xx} & r_{xy} \\ r_{xy} & r_{yy} \end{pmatrix} \quad (11)$$

where the $g(x, y)$ is the 2D Gaussian template. $Z(x, y)$ is the pixel of the image.

2) The subpixel position of the center point of the stripe can be obtained by Taylor expansion along the normal direction. Suppose the point (x_0, y_0) is the basis-point of the unit vector (n_x, n_y) of the Hessian matrix. Then, the gray level information of the point $(x_0 + tn_x, y_0 + tn_y)$ on the cross-section of the stripe can be derived by second order Tailor expansion of gray distribution function.

$$z(x_0 + tn_x, y_0 + tn_y) = Z(x_0, y_0) + N(r_x, r_y)^T + (tn_x tn_y) H(x, y) (tn_x tn_y)^T / 2 \quad (12)$$

where $\begin{cases} r_x = (\partial g(x, y)/\partial x) \otimes z(x, y) \\ r_y = (\partial g(x, y)/\partial y) \otimes z(x, y) \end{cases}$.

Let $\partial Z/\partial t = 0$,

$$t = -\frac{n_x r_x + n_y r_y}{n_x^2 r_{xx} + 2n_x n_y r_{xy} + n_y^2 r_{yy}} \quad (13)$$

The precise position of the center points of the stripe is $(x_0 + tn_x, y_0 + tn_y)$. Then, we can extract the centerline of the stripe. The result is shown in Figure 8. It can be seen that there exists a cluster on the both ends.

The Hessian matrix of the stripe is obtained by convolution with the corresponding differential Gaussian kernel

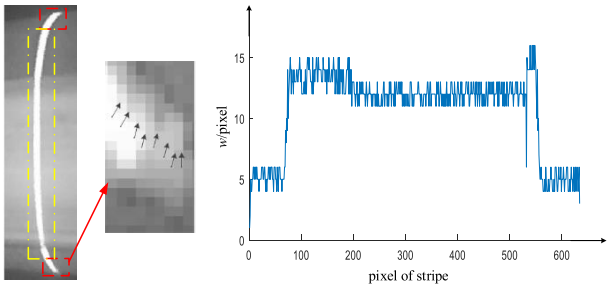

FIGURE 9. Segmentation of laser stripe.

function.

$$\begin{cases} r_x = \dfrac{-x \times e^{-\frac{x^2+y^2}{2\sigma^2}}}{\sigma^2 \times 2\pi\sigma^2} \\ r_y = \dfrac{-y \times e^{-\frac{x^2+y^2}{2\sigma^2}}}{\sigma^2 \times 2\pi\sigma^2} \\ r_{xx} = \left(\dfrac{x^2}{\sigma^4} - \dfrac{1}{\sigma^2}\right) \times \dfrac{e^{-\frac{x^2+y^2}{2\sigma^2}}}{2\pi\sigma^2} \\ r_{xy} = \dfrac{xy}{\sigma^4} \times \dfrac{e^{-\frac{x^2+y^2}{2\sigma^2}}}{2\pi\sigma^2} \\ r_{yy} = \left(\dfrac{y^2}{\sigma^4} - \dfrac{1}{\sigma^2}\right) \times \dfrac{e^{-\frac{x^2+y^2}{2\sigma^2}}}{2\pi\sigma^2} \end{cases} \tag{14}$$

where σ is the mean square deviation of Gaussian function. According to equation (14), we find that σ determines the effect of image smoothing filter. Traditional Steger algorithm uses the maximum of the stripe width w to calculate σ, that is

$$\sigma \geq \frac{w}{\sqrt{3}} \tag{15}$$

As shown in Figure 9, the width of laser stripes is inconsistent. The width of both ends is narrower than the middle. However, the traditional Steger algorithm considers the stripe width as a whole to extract the centerline. Thus induces the both ends of the stripe blurred.

To solve the problem, we modify the traditional method with flexible-widths Gaussian template. According to the distribution of the width pixel, first, we divide the whole stripe into three segments. Then, calculate the corresponding σ with different segment width. Last, we extract the centerline of each segment, and merge them together. The result is shown in Figure 10. Compared with the one shown in Figure 8, it can be seen that the both ends of laser stripe are located accurately.

D. LOCATION OF STRIPE ENDPOINTS AND RAILHEAD BOUNDARY DEFINITION

After extracting the centerline of the stripe, the four endpoints of the laser stripes depicted with blue and the two railhead boundaries depicted with green are shown in Figure 11.

E. LOCATION OF LASER MEASURING POINTS AND DEVIATION MEASUREMENT

First, referring to [15], we remove the 2D perspective distortion for this image. Then, the method of laser stripes region

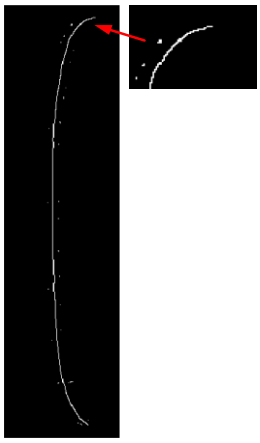

FIGURE 10. Extraction of laser stripe centerline by modified Steger algorithm.

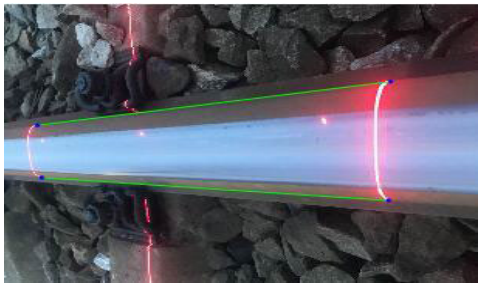

FIGURE 11. The endpoint of the strips and the railhead boundary.

FIGURE 12. Location of laser measuring points.

location is also suitable for the laser measuring point. After a coarse-to-fine processing, we search the laser points with empirical conditions equation (16) between the stipe boundaries. The result is shown in Figure 12.

$$R_{height} < \beta \cdot I_{width} \tag{16}$$

Last, we calculate the position deviations [15] using (17).

$$w_{dev} = \left(\frac{D_p}{D_b} - \frac{1}{2}\right) \times w_{rail} \tag{17}$$

where D_p is the distance between measuring point and the railhead upper boundary, D_b is the distance between the two boundaries, and w_{rail} is the true rail width.

IV. EXPERIMENT RESULTS AND DISCUSSIONS

In this section, first, we perform the static test and performance comparison with related methods to show the validity

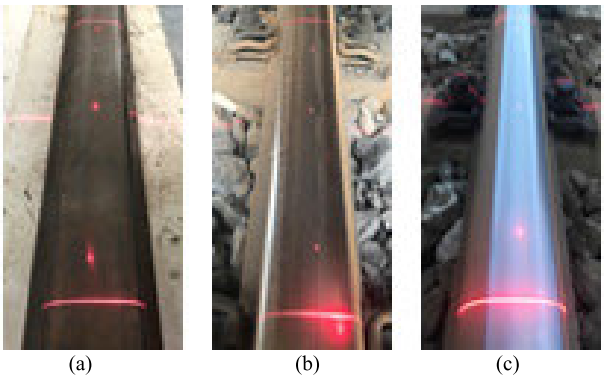

FIGURE 13. Three types of rails. (a) Original rail. (b) Rail in service. (c) Rail after milling.

of deviations calculation method. Then, we perform the dynamic test to prove the stability and repeatability of the proposed method. Finally, we analyze the system real-time performance further.

A. EXPERIMENT SETUP

The root-mean-square error (RMSE) and mean absolute error (MAE) are two widely used criteria in accuracy test [17].

$$\begin{cases} RMSE = \sqrt{\frac{1}{N}\sum_{i=1}^{N}\left(x_i - \hat{x}_i\right)^2} \\ MAE = \frac{1}{N}\sum_{i=1}^{N}\left|x_i - \hat{x}_i\right| \end{cases} \tag{18}$$

where N refers to the number of testing samples, x_i and $\hat{x}_i$ are the true position deviation values and measured position deviation values of the measuring point, respectively.

The test data is collected from three typical rail forms including original rail, rail in service and rail after milling, respectively. As shown in Figure 13, they almost include all possible rail surface reflection properties.

B. STATIC VALIDITY TEST

1) DIFFERENT POSITION DISTRIBUTIONS OF LASER MEASURING POINTS

We collected 600 images from three types of rail. Each rail type has 200 images. To verify the robustness of location of laser measuring points, for each form, as shown in Figure 14, we test with four different position distributions.

The results are summarized in Table 2. It can be seen that the results are basically consistent. Overall, the maximal error is not larger than 0.4 mm, which indicates the position distributions of the chord-based measuring point in the image has little effect on the results.

2) DIFFERENT POSITION DISTRIBUTIONS OF LASER STRIPES

Similar to the test above, to verify the robustness of location of laser stripe endpoints, we collected another 150 images with different position distributions of the laser stripes. As shown in Figure 15, the whole data is divided into four groups.

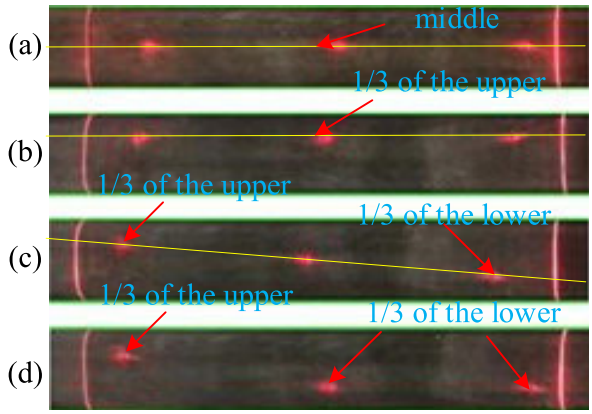

FIGURE 14. Four different position distributions of measuring points. (a)Test-I: points in the middle of the rail surface. (b) Test-II: points in the 1/3 of the rail surface. (c) Test-III: The line of points is inclined. (d) Test-IV: points are noncollinear.

TABLE 2. Measurment error of different position of measuring points.

	original rail		rail in operation		rail after milling	
	MAE	RMSE	MAE	RMSE	MAE	RMSE
Test-I	0.153	0.164	0.321	0.328	0.244	0.274
Test -II	0.193	0.204	0.253	0.232	0.391	0.346
Test -III	0.205	0.236	0.254	0.269	0.385	0.404
Test -IV	0.334	0.365	0.318	0.381	0.226	0.265

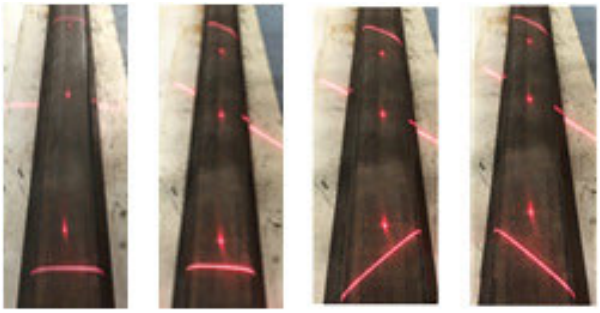

FIGURE 15. Different position distributions of laser stripes. (a)Group-I: position of stripes is normal. (b)Group-II: one stripe is inclined (c) Group-III: two stripes are inclined in different directions. (d) Group-IV: two stripes are inclined in same direction.

TABLE 3. Measurment error of different poistion of laser stripes in original rails test-I.

	MAE	RMSE
Group-I	0.253	0.264
Group -II	0.296	0.308
Group -III	0.228	0.246
Group -IV	0.253	0.272

The results are summarized in Table 3. It indicates that the position distributions of laser stripes have little effect on this system.

3) PERFORMANCE OF THE NIGHT MODE

To verify the performance that the system can work day and night, as shown in Figure 16(a), we collected 200 images

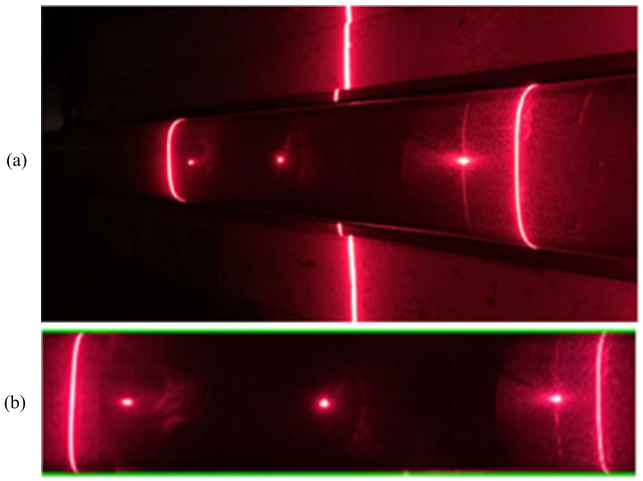

FIGURE 16. Working in night mode. (a) Origin image. (b) After processing.

TABLE 4. Measurment error of the night mode in original rails.

	MAE	RMSE
Test-I	0.347	0.357
Test -II	0.286	0.290
Test -III	0.131	0.145
Test -IV	0.265	0.268

in the night with four different positions distributions of the measuring points. The results of position deviations are summarized in Table 4.

From Table 4, the accuracy of measurement of position deviation in the day time is slightly better than in the night time, because the diffuse reflection of the laser stripes influences the accuracy of the rail boundary extraction. However, we can observe that the measurement errors obtained in the night are close to the ones in the day. It indicates that our method can work well in the night mode and is insensitive to the illumination. It could improve the operation efficiency greatly.

C. PREFORMANCE COMPARISON WITH RELATED MEDTHOD

1) COMPARISON OF CENTERLINE EXTRACTION METHODS

The centerline extraction is very important for the correct extraction of railhead boundary. Taking the stripe image shown in Figure 7(b) as an example, we compare our method with other methods, including skeleton refinement [18], [19] and traditional Steger algorithm [20], [21]. The skeleton refinement first uses refinement processing in mathematics morphology, and then extracts the skeleton of the stripe. However, there are many fringe breakpoints and burrs in the result shown in Figure 17(a), especially in the arc area of the rail surface. The traditional Steger algorithm considers the stripe width as a constant value to extract the centerline. The pixels are accumulational at the both ends of the centerline shown in Figure 17(b). By contrast, the details of the endpoints are

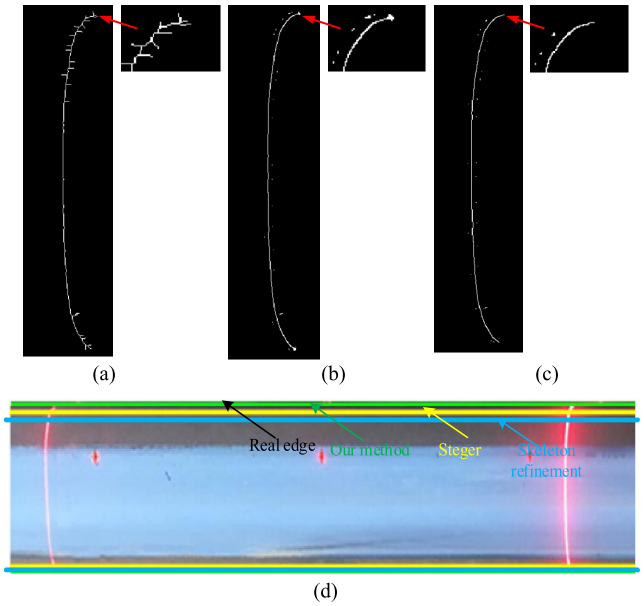

FIGURE 17. Comparison of centerline extraction methods. (a) Skeleton refinement. (b)Steger algorithm. (c)Our method. (d) Result after skew correction.

preserved well by our method in Figure 17(c), which can be utilized effectively to help find the true boundary.

Further, we set the far right points at both ends of the stripe as the endpoints for Skeleton refinement, and the center of mass of the cumulative pixels at both ends as the endpoints for Steger algorithm. The railhead boundaries are depicted in Figure 17(d). Obviously, the error of the skeleton refinement method and traditional Steger algorithm is larger than our method.

2) COMPARISON OF BOUNDARY EXTRACTION METHODS

Graph Cut is a classical edge detection and image segmentation algorithm for region extraction. We compare it and our previous work [15] with proposed method in this paper. We collected another 600 images on the three typical rail forms with four different positions of the measuring point.

a: GRAPH CUT

The graph cut algorithm adopts the max-flow min-cut to optimize the modeling in the background segmentation, the stereo images matching and image matting [22], [23]. Treat the railhead surface image as a matrix, the single pixel of the image is a position in the matrix, and this pixel can be regarded as a vertex in the image. Then, the edges are formed by connecting the adjacent vertexes with short line. According to the weight of edge, the image can be divided into foreground and background. As shown in Figure 18, the railhead surface is the foreground, and the rest is the background.

b: EDGE DETECTION COMBINED WITH HOUGH TRANSFORM ALGORITHM [15]

Edge detection algorithms such as Canny operator, differential operator and Laplace operator have been widely used in

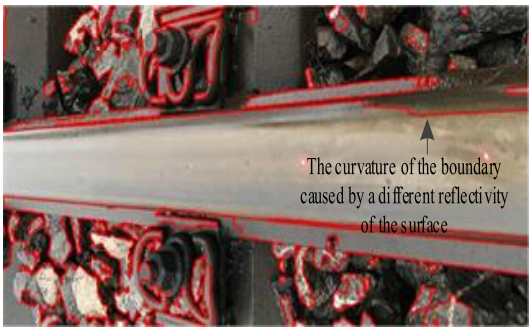

FIGURE 18. Image segmentation by graph cuts.

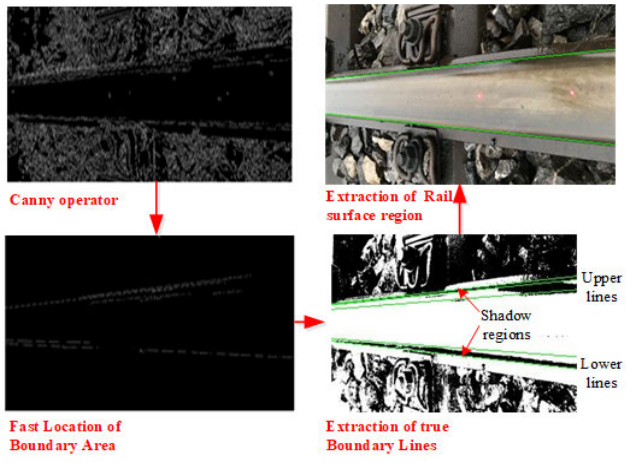

FIGURE 19. Image segmentation by edge detection combined with Hough transform algorithm.

various fields of image detection. Therefore, it is feasible to extract the railhead surface region. As shown in Figure 19, the process of edge detection combined with Hough transform algorithm is as follow: image contrast enhancement by HF, fast location of boundary area, fitting of underlying boundary lines, and final extraction of true boundary lines.

The comparison of different boundary extraction methods is summarized in Table 5. As a whole, the accuracy of Graph cut is the worst. The influence of unequal illumination and the reflection property of rail surface cause this situation. The edge detection combined with Hough transform algorithm (reference [15] method) is much better than the Graph Cut, but in the detection of the rail in operation and the rail after milling, the smooth contact area affects the measurement accuracy. By contrast, the accuracy of our method is the highest, because that the variable working condition has little effect on the location of laser stripes.

D. DYNAMIC TEST

In order to verify the stability and repeatability of the proposed method, we conduct the outdoor dynamic test with the hand-push measurement platform shown in Figure 20(a). The test is carried out in an outdoor 50kg/m railway. The length of the test line is about 100m, and includes the turnout zone whose length is 45m and the general track zone whose length is 55m.

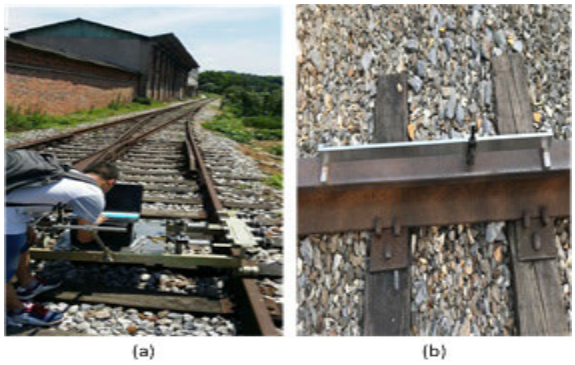

FIGURE 20. The field test and rail corrugation gauge test. (a) Field test. (b) Rail corrugation gauge test.

First, we collected 100m true values by manual measurement with the rail corrugation gauge, as shown in Figure 20(b). Then, on the same zone, we collect the corrugation values without operating of calibration to serve as the preprocessing result. If the corrugation value could not be measured because of the deviation of the measuring points in the curve rails, the values are assigned 1 directly, which is far higher than the normal value. Finally, we compare our method and the reference [15] method using the corrugation values with different speed.

The qualitative and quantitative result comparisons are shown in Figure 21 and Table 6, respectively. Without calibration, the measured corrugation is influenced visibly. Compare with the true corrugation values, the MAE and RMSE reached to 0.5801 and 0.3786, respectively. However, after the calibration by reference [15] and our method, the error is reduced dramatically. Compared reference [15], our method can achieve a better tracking performance at the beginning of the curve zones. Meanwhile, the results are robust to the vehicle speed.

In the state-of-art methods, Li and Shi [24] in 2019 proposed the measurement model based on inertial reference method, which is use the fiber laser accelerometers. The measurement (99%) accuracy of rail corrugation depth is about 0.04mm. Teng *et al.* [25] in 2020 proposed the 2D-RCM measurement system for rail corrugation. This method splices the corrugation measurement data collected by 2D displacement sensor. The RMSE of the rail corrugation is between 0.03mm and 0.06mm. According to our dynamic test, the RMSE of the values of rail corrugation is about 0.02mm in our system. To summarize, our system reaches the advanced level of fellow products.

E. REAL-TIME PERFORMANCE TEST

We test the actual run time for the system based on our method. This experiment was carried on a desktop with an Intel Core i5 CPU (3.2 GHz) and 4 GB memory. The program was implemented with Visual C++. The mean run time of a rail image is about 80 ms, and is only 2/3 of the time required by the reference [15] method. The reason is that we use partial processing of the image instead of the whole image

TABLE 5. Comparison of railhead boundary extraction methods.

	Graph Cuts			reference [15] method			Our method		
	Original rail	rail in operation	Rail after milling	Original rail	rail in operation	Rail after milling	Original rail	rail in operation	Rail after milling
Test-I	0.741	1.177	1.599	0.221	0.229	0.472	0.164	0.328	0.274
Test-II	0.493	0.776	1.465	0.224	0.355	0.509	0.204	0.232	0.346
Test-III	0.927	1.036	1.655	0.326	0.365	0.506	0.236	0.269	0.404
Test-IV	0.514	0.891	1.371	0.375	0.383	0.565	0.365	0.381	0.265

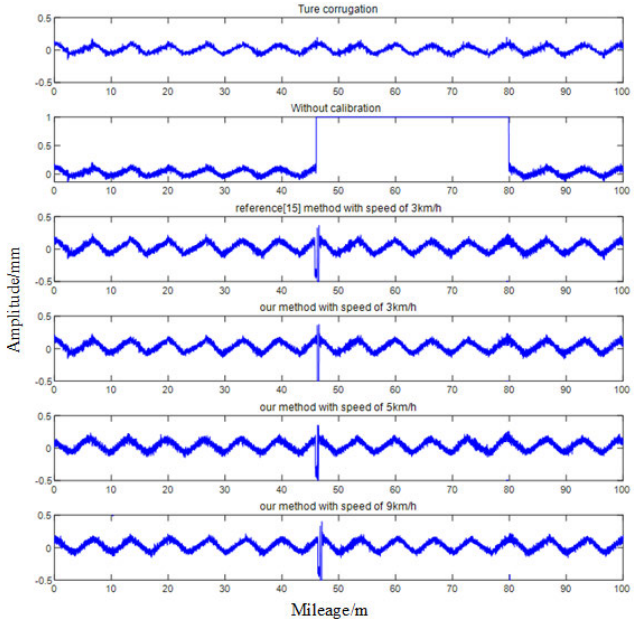

FIGURE 21. Result comparison between true corrugation values, corrugation without calibration, and the corrugation with calibration.

TABLE 6. Validity test of dynamic operation.

	Without calibration	Reference [15] method with 3km/h	Our method with 3km/h	Our method with 5km/h	Our method with 9km/h
RMSE	0.5801	0.0362	0.0180	0.0295	0.0386
MAE	0.3786	0.0214	0.0106	0.0140	0.0233

processing. Further, we can derive that the average detection speed of proposed system is about 9 km/h, which is far higher than that of the rail maintenance train (up to 5 km/h).

V. CONCLUSION

We have proposed a bi-linear laser assisted method to locate the railhead boundary and measure the position deviations of chord-based rail corrugation measuring points. Compared with state of the art methods, the most significant breakthrough is that this method is insensitive to the illumination and reflection property of the rail surface. Thus makes it could work day and night, without the assistance of additional light source.

In the experiment, the accuracy of the position deviation measurement is limited within 0.4 mm, and the position distributions of the laser measuring points and laser stripes have little effect on the result. Further, we compare our centerline extraction method with skeleton refinement and traditional Steger algorithm. The results show that the Steger algorithm with varying widths Gaussian template is better.

ACKNOWLEDGMENT

The authors would like to thank the editors and anonymous reviewers for their careful work and thoughtful suggestions that have helped to improve this article substantially.

REFERENCES

[1] S. L. Grassie, "Rail corrugation: Advances in measurement, understanding and treatment," *Wear*, vol. 258, nos. 7–8, pp. 1224–1234, Mar. 2005.
[2] Z. Ma, Y. Dong, H. Liu, X. Shao, and C. Wang, "Forecast of non-equal interval track irregularity based on improved grey model and PSO-SVM," *IEEE Access*, vol. 6, pp. 34812–34818, 2018.
[3] M. Hiensch, J. C. O. Nielsen, and E. Verheijen, "Rail corrugation in The Netherlands—Measurements and simulations," *Wear*, vol. 253, nos. 1–2, pp. 140–149, Jul. 2002.
[4] Y. Li, H. Liu, and Z. Ma, "Trend extraction of rail corrugation measured dynamically based on the relevant low-frequency principal components reconstruction," *Meas. Sci. Technol.*, vol. 27, no. 10, Oct. 2016, Art. no. 105005.
[5] Z. Liu, J. Sun, H. Wang, and G. Zhang, "Simple and fast rail wear measurement method based on structured light," *Opt. Lasers Eng.*, vol. 49, no. 11, pp. 1343–1351, Nov. 2011.
[6] Y. Wang, H. Tang, P. Wang, X. Liu, and R. Chen, "Multipoint chord reference system for track irregularity: Part I—Theory and methodology," *Measurement*, vol. 138, pp. 240–255, May 2019.
[7] B. An, L. Gao, T. Xin, G. Xiang, and J. Wang, "A novel approach of identifying railway track Rail's modal frequency from wheel-rail excitation and its application in high-speed railway monitoring," *IEEE Access*, vol. 7, pp. 180986–180997, 2019.
[8] M. Molodova, Z. Li, and R. Dollevoet, "Axle box acceleration: Measurement and simulation for detection of short track defects," *Wear*, vol. 271, nos. 1–2, pp. 349–356, May 2011.
[9] P. Salvador, V. Naranjo, R. Insa, and P. Teixeira, "Axlebox accelerations: Their acquisition and time–frequency characterisation for railway track monitoring purposes," *Measurement*, vol. 82, pp. 301–312, Mar. 2016.
[10] Y. Li, H. Liu, Z. Ma, C. Wang, and X. Zhong, "Rail corrugation broadband measurement based on combination-chord model and LS," *IEEE Trans. Instrum. Meas.*, vol. 67, no. 4, pp. 938–949, Apr. 2018.
[11] C. Wang and J. Zeng, "Combination-chord measurement of rail corrugation using triple-line structured-light vision: Rectification and optimization," *IEEE Trans. Intell. Transp. Syst.*, early access, Jul. 8, 2020, doi: 10.1109/TITS.2020.3004918.

[12] *Railway Applications-Noise Emission-Rail Roughness Measurement Related to Rolling Noise Generation*, Standard BS EN 15610-2009, British Standard Inst., London, U.K., European Committee Standardization, 2009.
[13] *Railway Applications. Track. Acceptance of Works Part 3: Acceptance of Reprofiling Rails in Track*, Standard BS EN 13231-3:2012, European Committee Standardization, British Standard Inst., London, U.K., 2012.
[14] H. Li, J. Chen, and Y. Ren, "Study on detection system of metro rail corrugation," *Wireless Internet Technol.*, no. 5, pp. 80–82, May 2014.
[15] L. Chen, Y. Li, X. Zhong, Q. Zheng, and H. Liu, "An automated system for position monitoring and correction of chord-based rail corrugation measuring points," *IEEE Trans. Instrum. Meas.*, vol. 68, no. 1, pp. 250–260, Jan. 2019.
[16] Q. Meng, X. Wen, L. Yuan, and H. Xu, "Factorization-based active contour for water-land SAR image segmentation via the fusion of features," *IEEE Access*, vol. 7, pp. 40347–40358, 2019.
[17] T. Fawcett, "An introduction to ROC analysis," *Pattern Recognit. Lett.*, vol. 27, no. 8, pp. 861–874, Jun. 2006.
[18] Z. Huang, "Fringe skeleton extraction using adaptive refining," *Opt. Lasers Eng.*, vol. 18, no. 4, pp. 281–295, Jan. 1993.
[19] T. Yu, J. Zhao, Y. Huang, Y. Li, and Y. Liu, "Towards robust and accurate single-view fast human motion capture," *IEEE Access*, vol. 7, pp. 85548–85559, 2019.
[20] R. Yang, S. Cheng, W. Yang, and Y. Chen, "Robust and accurate surface measurement using structured light," *IEEE Trans. Instrum. Meas.*, vol. 57, no. 6, pp. 1275–1280, Jun. 2008.
[21] R. Xiao, Y. Xu, Z. Hou, C. Chen, and S. Chen, "An adaptive feature extraction algorithm for multiple typical seam tracking based on vision sensor in robotic arc welding," *Sens. Actuators A, Phys.*, vol. 297, Oct. 2019, Art. no. 111533.
[22] S. M. Ben, A. Mitiche, and A. I. Ben, "Multiregion image segmentation by parametric kernel graph cuts," *IEEE Trans. Image Process.*, vol. 20, no. 2, pp. 545–557, Feb. 2011.
[23] C. A. Sciammarella and L. Lamberti, "Mathematical models utilized in the retrieval of displacement information encoded in fringe patterns," *Opt. Lasers Eng.*, vol. 77, pp. 100–111, Feb. 2016.
[24] J. Li and H. Shi, "Rail corrugation detection of high-speed railway using wheel dynamic responses," *Shock Vibrat.*, vol. 2019, pp. 1–12, Feb. 2019.
[25] Y. Teng, H. Liu, J. Liu, C. Wang, and Z. Ma, "A rail corrugation measurement method based on data splicing," *Measurement*, vol. 156, May 2020, Art. no. 107560.

LIANG CHEN received the B.Sc. degree in electronic information engineering from the North University of China, Taiyuan, China, in 2016. He is currently pursuing the Ph.D. degree with the College of Control Science and Engineering, Zhejiang University, Hangzhou, China.

His current research interests include machine learning, railway inspection, and signal processing.

YANFU LI received the B.Sc. and Ph.D. degrees in electrical engineering from Hunan University, Changsha, China, in 2011 and 2018, respectively.

He is currently an Assistant Professor with the Air Force Engineering University. His current research interests include machine learning, railway inspection, and signal processing.

ZIJI MA received the B.Sc. degree in electronic information engineering from Hunan University, Changsha, China, in 2001, and the Ph.D. degree in information science from the Nara Institute of Science and Technology, Nara, Japan, in 2012.

He is currently an Associate Professor with Hunan University. His current research interests include machine vision, railway inspection, and signal processing.

HONGLI LIU received the B.Sc. degree in electrical engineering and the Ph.D. degree in control theory and engineering from Hunan University, Changsha, China, in 1985 and 2000, respectively.

He is currently a Professor and the Department Head with the College of Electrical and Information Engineering, Hunan University. His current research interests include intelligent information processing and transmission technology.

WEIJIE MAO received the B.Sc. degree in electrical engineering and the Ph.D. degree in control science and engineering from Zhejiang University, Hangzhou, China, in 1991 and 1996, respectively.

He is currently a Professor with Zhejiang University. His current research interests include modeling, control and optimization of complex systems, machine vision, and machine learning.